Supporting Information

High-Frequency Graphene Base Hot-Electron Transistor

Bor-Wei Liang,¹ Wen-Hao Chang,¹ Hung-Yu Lin, Po-Chun Chen, Yi-Tang Zhang, Kristan Bryan Simbulan, Kai-Shin Li, Jyun-Hong Chen, Chieh-Hsiung Kuan,^{*} and Yann-Wen Lan^{*}

Corresponding Authors

Chieh-Hsiung Kuan - Email: chkuan@ntu.edu.tw

Yann-Wen Lan - Email: ywlan@ntnu.edu.tw

Keywords: hot-electron transistor, radio frequency electronics, two-dimensional materials, hot carriers, tunneling electronics.

1. Morphological and spectroscopic characterizations of graphene and MoS₂.

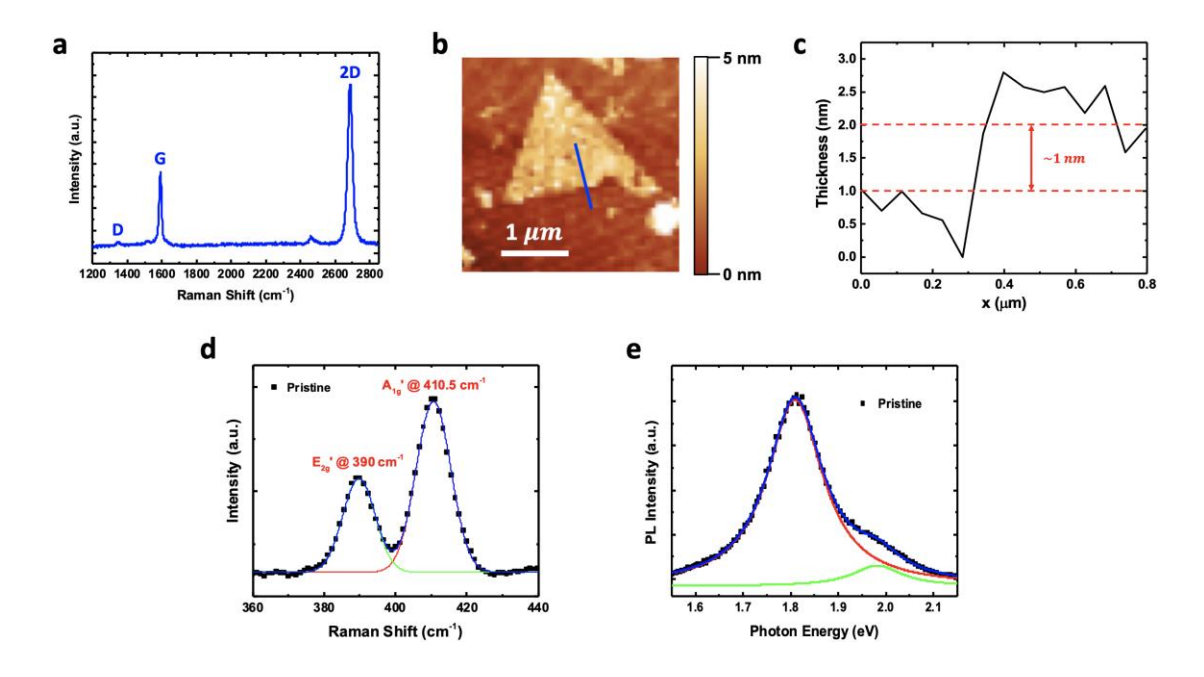


Figure S1. (a) Raman spectrum of monolayer CVD-grown graphene. (b) AFM image of the MoS_2 sample. (c) The thickness of transferred monolayer MoS_2 is ~ 1 nm. (d) Raman and (e) photoluminescence (PL) spectra of the monolayer CVD-grown MoS_2 .

We have measured the morphological and spectroscopic characterizations of both graphene and MoS_2 which were used in fabricating our devices as shown in Figure S1a-d. Figure S1a clearly shows the ratio between the G and 2D peaks (about 1:2) with a weak defect peak, indicating an almost perfect single layer graphene (SLG).¹ The thickness of the transferred monolayer MoS_2 (~1 nm) is analyzed from the AFM image as shown in Figure S1 (b-c). In Figure S1 (d), the peak separation of Raman peaks A_{1g} and E_{2g} is around 20.5 cm⁻¹ indicating a monolayer CVD- MoS_2 as well. Furthermore, the band gap energy of the MoS_2 sample's A exciton at around 1.8 eV also represents that of a monolayer MoS_2 as shown in Figure S1 (e).

2. Contact resistance between graphene and base electrode.

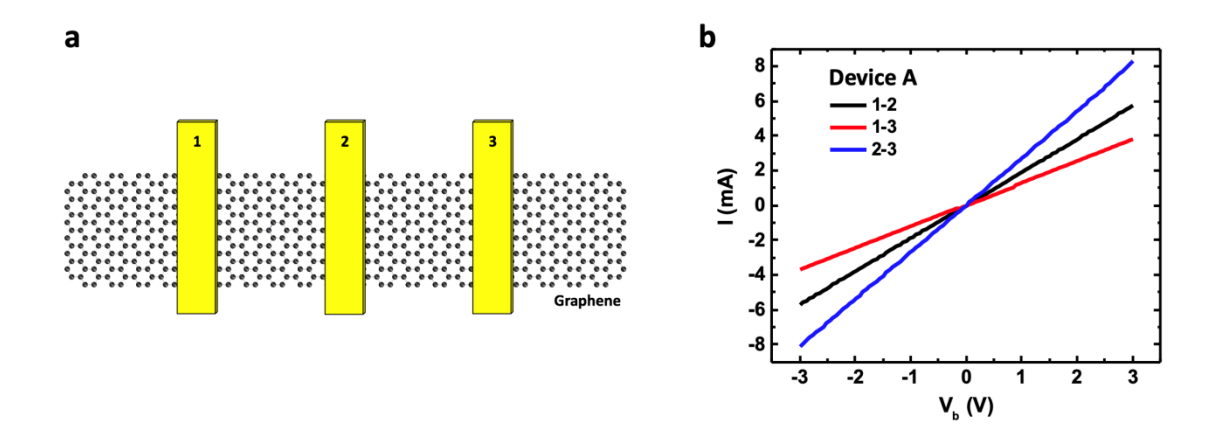


Figure S2. (a) Schematic illustration of multi-electrode graphene devices. Three Ti/Au electrodes are deposited on top of monolayer graphene sheet to measure and calculate the contact resistance. (b) IV characteristics of device A for different pairs of electrodes showing ohmic contact behaviors.

Table S1. Measured $(R_{1,2}, R_{1,3}, R_{2,3})$ and calculated (R_{C2}) contact resistances of two multi-electrode graphene devices.

	$R_{1,2}(\Omega)$	$R_{1,3}\left(\Omega\right)$	$R_{2,3}\left(\Omega\right)$	$R_{C2}(\Omega)$
Device A	0.37k	1.06k	0.78k	45
Device B	0.52k	0.79k	0.37k	50

Two multi-electrode graphene devices were fabricated, as shown in the schematic illustration of Figure S2 (a) to confirm the ohmic contact between the base graphene and the contact metal. Figure S2 (b) presents the two-terminal IV measurement of device A showing good ohmic behaviors. The contact resistances R_{C2} are around 45

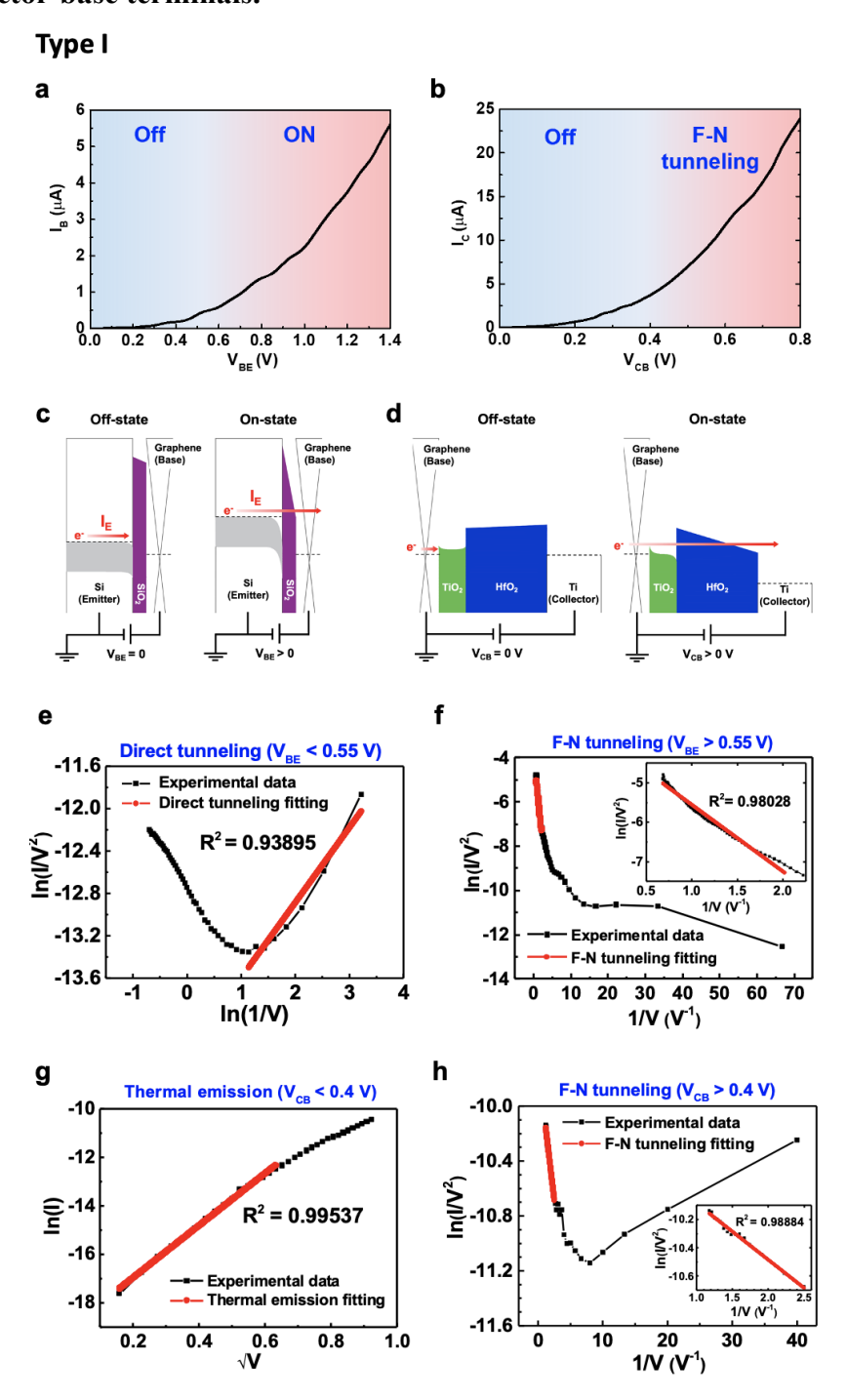
ohm and 50 ohm for device A and device B, respectively, which are calculated by the following equations³ and are similar to other references.^{4,5}

$$R_{Cn} = (R_{n-1,n} + R_{n,n+1} - R_{n-1,n+1})/2$$
 (E1)

$$R_{C2} = (R_{1,2} + R_{2,3} - R_{1,3})/2$$
 (E2)

The measured resistances $(R_{1,2}, R_{1,3}, R_{2,3})$ and calculated contact resistances (R_{C2}) for both devices A and B are shown in Table S1.

3. Two-terminal measurements of type I and type II device's emitter-base and collector-base terminals.



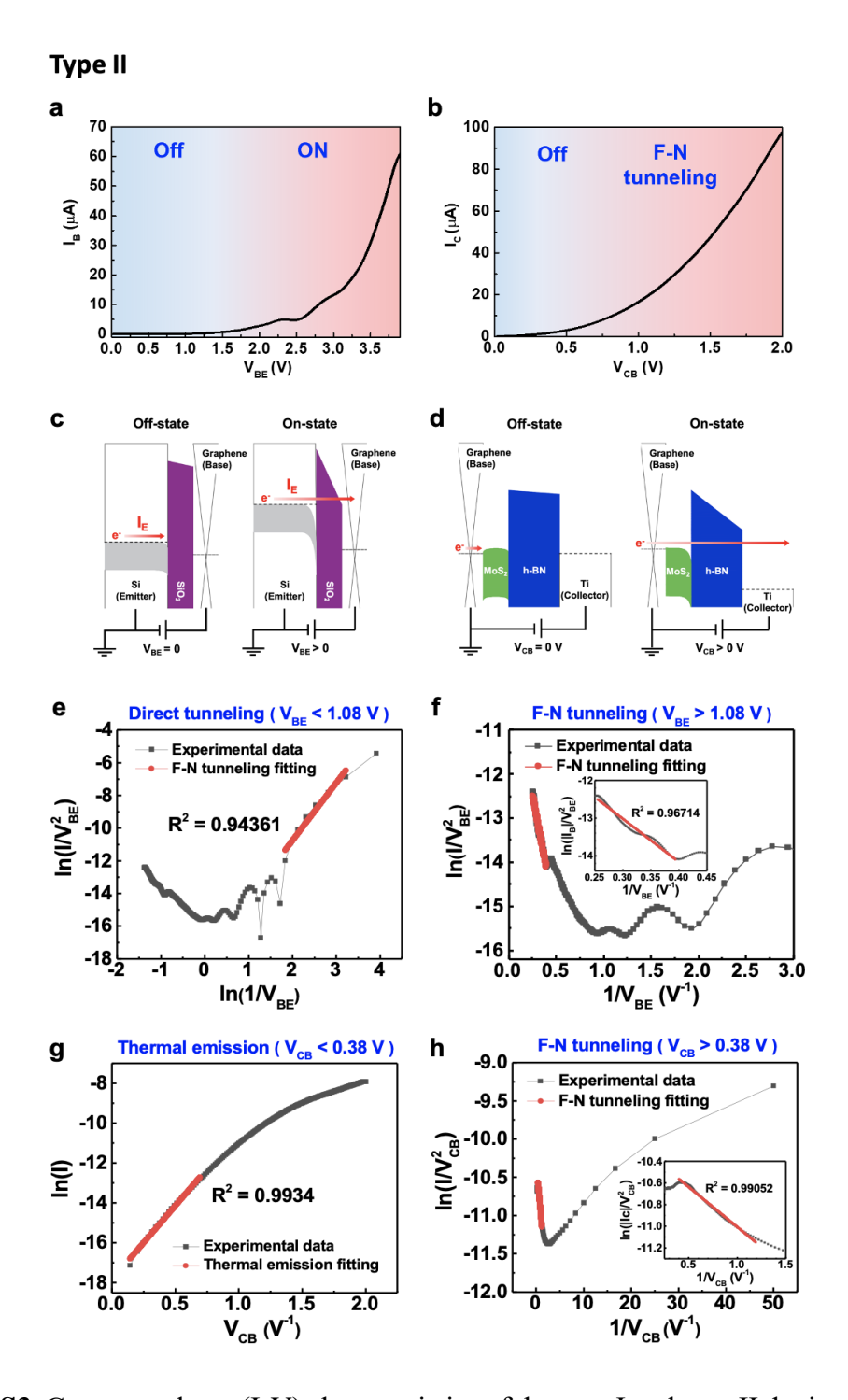


Figure S3. Current-voltage (I-V) characteristics of the type I and type II devices in two-terminal measurement for the (a) emitter and base and for the (b) base and collector terminals. Schematic energy band diagram of the on-state and off-state conditions (c) for B-E terminals and (d) B-C terminals. Linear fitting of (e) Direct tunneling and (f) Fowler—Nordheim (F-N) tunneling for the E-B terminal, and that of (g) thermal emission and (h) F-N tunneling for the B-C terminal.

To check the quality of emitter and base barrier, two-terminal current-voltage characteristics involving both the B-E and the B-C barriers should be studied first. Figure S3 (a) shows the current-voltage (I-V) characteristics measurement for the base current (emitter current) as a function of the emitter injection bias V_{BE}. The onset voltage V_{on} is around 0.5 V and the current levels after the onset are a few tens of microamperes with a current density of ~ few ten A/cm². Figure S3 (b) shows the basecollector current as a function of base control bias VCB where similar characteristics as that of Figure S3 (a) are demonstrated but with an onset voltage V_{on} of around 0.4 V. These on-off characteristics revealed by the B-E and B-C terminals measurement through a tunnel barrier can arise from several potential mechanisms. Figure S3 (c) plots the schematic energy band diagram of the off-state and on-state conditions across the B-E terminals; while Figure S3 (d) displays the schematic energy band diagram of the off-state and on-state conditions for the B-C terminals. As implied in these diagrams, the transport characteristic is dominated by the quantum mechanical tunneling mechanism of electrons. Due to the applied bias, energy filter barriers can be controlled to further switch between the on-state and the off-state of the two pairs of terminals.

In order to confirm the operating bias region of the device, the tunneling mechanisms of the carriers from the emitter, through the base, to the collector should be well studied. Carrier transport through a tunnel barrier above the onset voltage can arise from several mechanisms such as Direct Tunneling, Fowler–Nordheim (F-N) tunneling, and Thermal Emission (TE).

For the B-E terminal, the I-V relationship curve of the Direct tunneling (off-state) mechanism can be linearly fit on an $ln(I/V^2)$ as a function of $ln(V^{-1})$ plot at $V_{BE} < 0.55$ V (Figure S3 (e)) while the I-V relationship curve of the F-N tunneling (on-state) mechanism can be analyzed on an ln(I) as a function of V^{-1} plot at $V_{BE} > 0.55$ V (Figure

S3 (f)).^{6, 7} This indicates the dominance of each of the mentioned mechanisms in separate ranges of V_{BE} . Consequently, the switch point in between the on- and the offstate is observed at V_{BE} = 0.55 V. Similar characteristics were also revealed across the C-B terminals.

For the C-B terminal, the I-V relationship curve of the thermal emission (off-state) mechanism can be linearly fit on an ln(I) as a function of $ln(V^{1/2})$ plot at $V_{CB} < 0.4$ V (Figure S3 (g)), while the I-V relationship curve of the F-N tunneling (on-state) mechanism can be studied on an ln(I) as a function of V^{-1} plot at $V_{CB} > 0.4$ V, (Figure S3 (h)). Similar results for type II GHET devices are shown in the bottom portion of Figure S3.

4. Two-terminal transport characteristics of type I devices for temperaturedependent measurement.

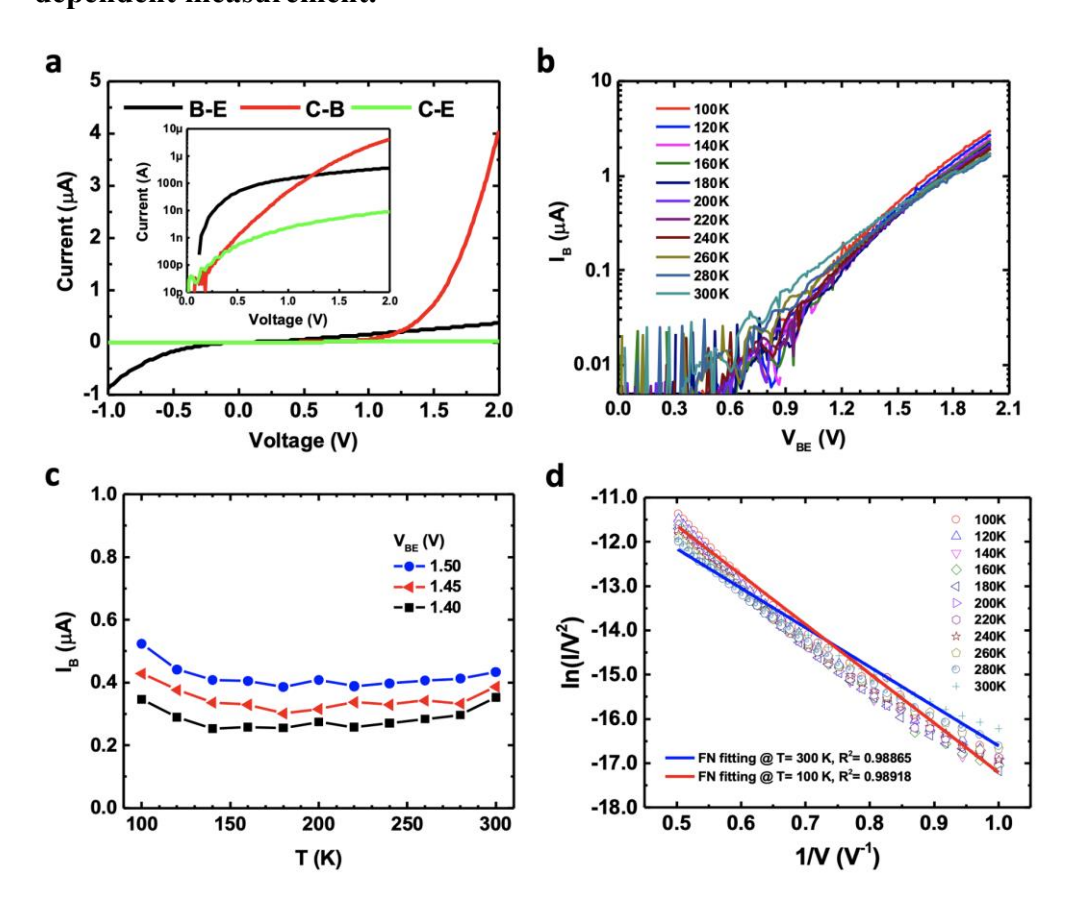


Figure S4. (a) Linear and logarithmic (inset) plots of the two-terminal IV characteristics of the device's B-E, C-B, and C-E junctions. (b) Temperature-dependent measurement of the B-E IV characteristics recorded from T= 100 K to T= 300 K. (c) The current I_B as a function of temperature T at fixed bias V_{BE}, indicating the domination of the tunneling mechanism. (d) FN tunneling fitting curves for T= 300 K and T= 100 K.

Two-terminal characteristics (B-E, C-B, and C-E) in another device have been measured as presented in Figure S4 (a). The current from the collector to the emitter (C-E) is negligible (\sim a few nA), suggesting low direct leakage. In addition, temperature-dependent measurements from T = 100 K to T = 300 K have been performed, as shown in Figure S4 (b) and (c), where we observed almost constant

current levels at different temperatures at certain fixed values of V_{BE} , confirming the tunneling mechanism. Furthermore, Fowler Nordheim model is also used to fit our experimental data at both T=300K and T=100K, showing a clear tunneling behavior with high coefficient of determination R^2 as shown in Figure S4 (d).

5. Energy band diagrams for different operating conditions of type I device.

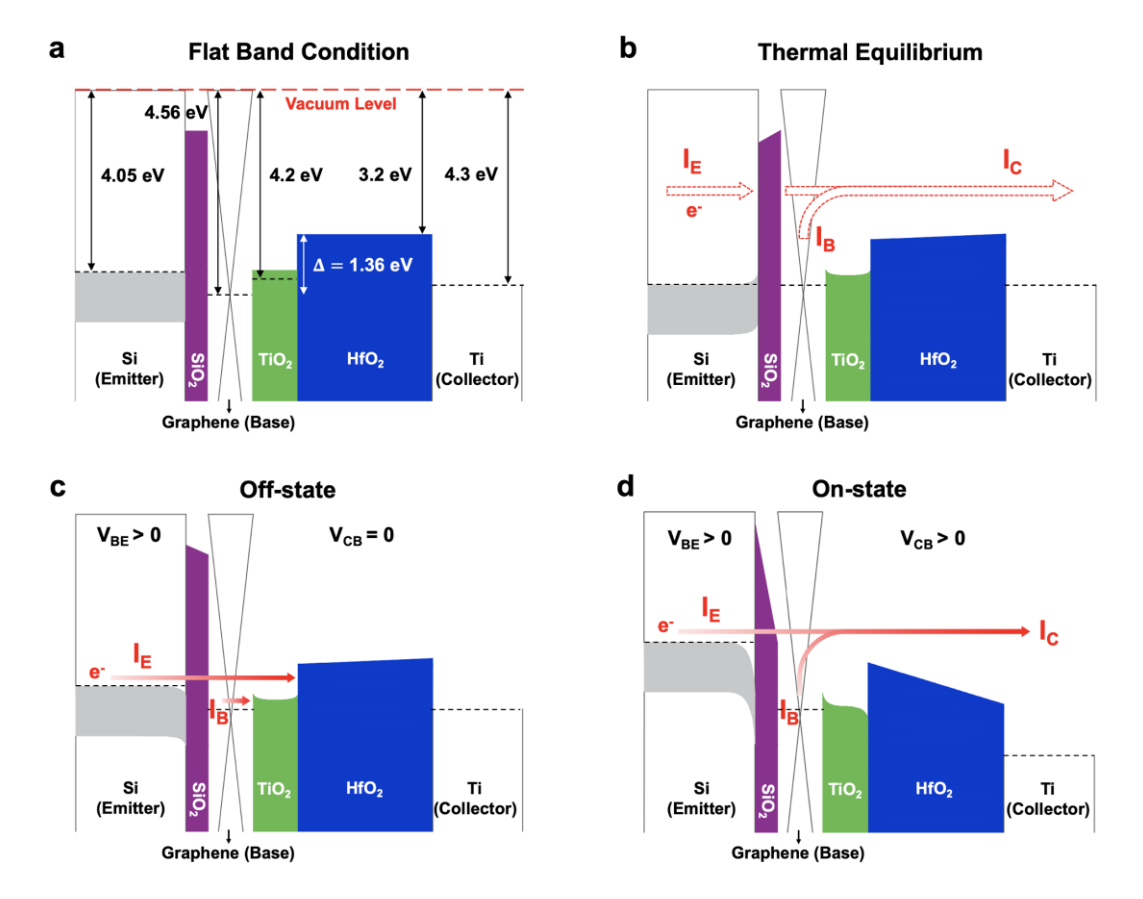


Figure S5. Energy band diagrams for different operating conditions of type I the graphene-base HET. (a) flat band condition, (b) thermal equilibrium condition, (c) off-state condition and (d) on-state condition.

The energy band diagrams for different operating conditions of type I graphene base HET (shown in Figure S5) is similar to that of type II device. The difference is the thicker CB barrier of the type II device (\sim 11 nm), which is substituted to TiO₂ (\sim 9 nm) and HfO₂ (\sim 30 nm).

6. DC three-terminal measurements for type I device.

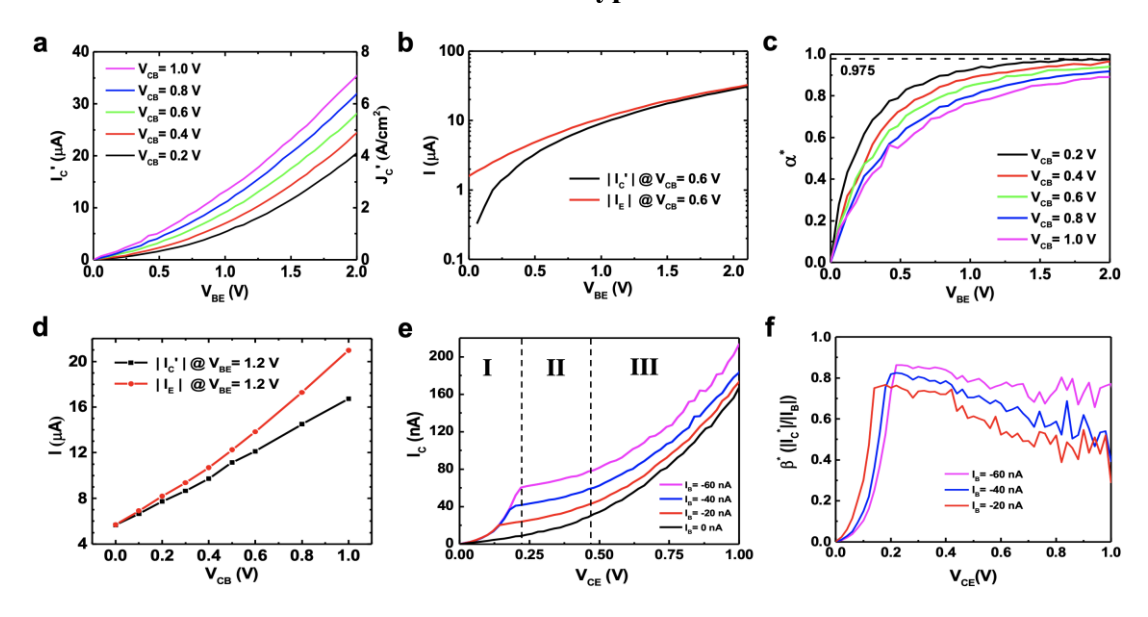


Figure S6. DC measurement result of type I device. (a) I-V_{BE} curves showing the output collector current (Ic') controlled by various values of V_{CB} under common base operation. (b) I-V_{CB} curves comparing the input emitter current (I_E) and the output collector current (Ic') at V_{CB} = 0.6 V. (c) Common base current gain (α^*) as a function of V_{BE} at various V_{CB} levels. (d) I-V_{CB} curves comparing the input emitter current (I_E) and the output collector current (Ic') at V_{BE} = 1.2 V. Common emitter characteristics for (e) collector current and (f) current gain (β^*) tuned by V_{CE} at varying input base current (I_B).

The common base and common emitter configurations of type I device are shown in Figure S6 (a-d) and Figure S6 (e-f) respectively. These behaviors are similar but inferior to that of type II device (as presented in Figure 3 in main text). The current density of type II device (J_c '~ 200 A/cm²), common base current gain (α *~ 0.992) and common emitter current (β *~ 2.7) are much higher than the performances of type I device (J_c '~ 7 A/cm², α *~ 0.975 and β *~ 0.8) which is demonstrated in Figure S6 (a), (c), and (f). This is owed to a lesser trap-mediated tunneling electrons and a smaller barrier width

in the CB barrier (MoS₂/h-BN) of type II device compared to that of type I device (TiO₂/HfO₂).

7. Extended data for DC three-terminal measurements of the type II device.

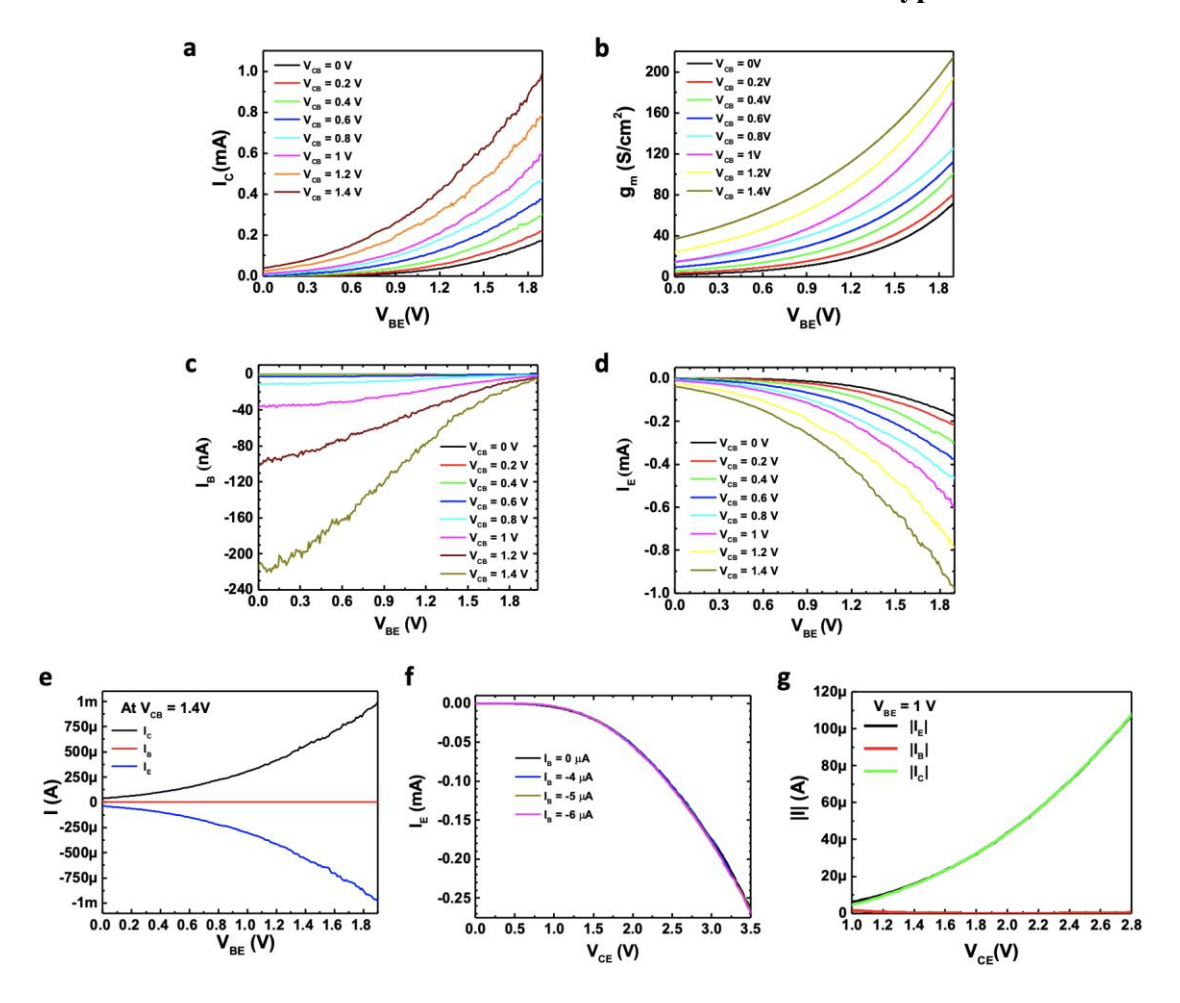


Figure S7. The (a) I_C, (b) transconductance (g_m), (c) I_B, and (d) I_E curves at various applied collector-base voltages, V_{CB}, in common base measurement. (e) The I_C, I_B and I_E characteristic for common base operation at V_{CB} = 1.4V. (f) I_E characteristic at different input current I_B by common emitter measurement. For our all electrical measurements, the emitter, base and collector currents are measured at the same time. (g) The I_C, I_B and I_E for common emitter operation at V_{BE} = 1V.

We always simultaneously measure the emitter, base and collector currents in our electrical measurement. Acquired from the common base measurement of type II GHET, Figure S7 (a) shows the collector current (I_C). The value of I_C (V_{BE} = 0 V, V_{CB} \neq 0 V) is smaller than 50 μ A, which is much smaller than I_C' (\sim 1 mA) at high V_{BC} bias

and at high applied V_{BE} (see Figure 3a in main text). This result indicates that the main component of collector current is dominated by hot electrons from the emitter instead of cold carriers from base. Figure S7 (b) shows the transconductance (g_m), which is calculated by exponential fitting (Ic, see Figure 3a in main text) as a function of V_{BE} at various fixed V_{CB}. A noticeable increase of g_m at larger V_{BE} indicates that the barrier of base-emitter is bent by the applied V_{BE} so that the hot electron can tunnel through emitter to base. The enhancement of gm modulated by VCB does not only reveal that hot electrons pass through the collector base barrier easily; but also indicate that the lower the base-emitter barrier, the more hot electrons flow from the emitter. Figure S7 (c) shows that the base current is almost constant as a function of VBE and is a few ten times smaller than Ic' (see Figure 3a in main text). Accordingly, it indicates that the electric field penetrates from emitter base junction into collector base junction. Owing to this strong penetration of electrical field from collector-base junction into emitterbase junction, an additional emitter current (I_E) can still be induced by applying V_{CB} (Figure S7 (d)). It is probably due to the thin graphene base and thin emitter-base barrier in the device. The bending of the emitter-base barrier is indeed affected by the increasing V_{CB}, which may cause an enhancement of I_E. In order to show the I_C mainly composed by the hot electrons from emitter, not from leakage base-collector current, the I_C , I_B and I_E characteristic at fixed $V_{CB} = 1.4V$ have demonstrated in Figure S7 (e). The value of I_C is much larger than I_B at high V_{BE} applied and the leakage current (I_C at V_{BE} = 0 V, ~ 40 μ A) is much smaller than collector current (~ 1mA). According to these results, we believe that the leakage base-collector current does not dominate the device.

Figure S7 (f) shows the I_E - V_{CE} characteristics obtained from the same common emitter measurement performed to get Figure 3e in main text. The lower current level of I_E at small values of V_{CE} is evidence that the kinetic energy of hot electrons is not

high enough to tunnel through the emitter-base barriers. While at higher V_{CE} , much more hot electrons get enough kinetic energy to tunnel across from emitter into the collector.

To clarify the RF measurement (see Figure 4 in main text) dominated by the emitter-collector current, we show I_E, I_B and I_C in common emitter DC measurement in Figure S7 (g) to indicate low I_B, implying that base-collector current is too small to dominate the transport. Therefore, we think emitter-collector current is in charge of the transport process in our devices.

8. The common base characteristic of both type I and type II devices in different input emitter current (I_E).

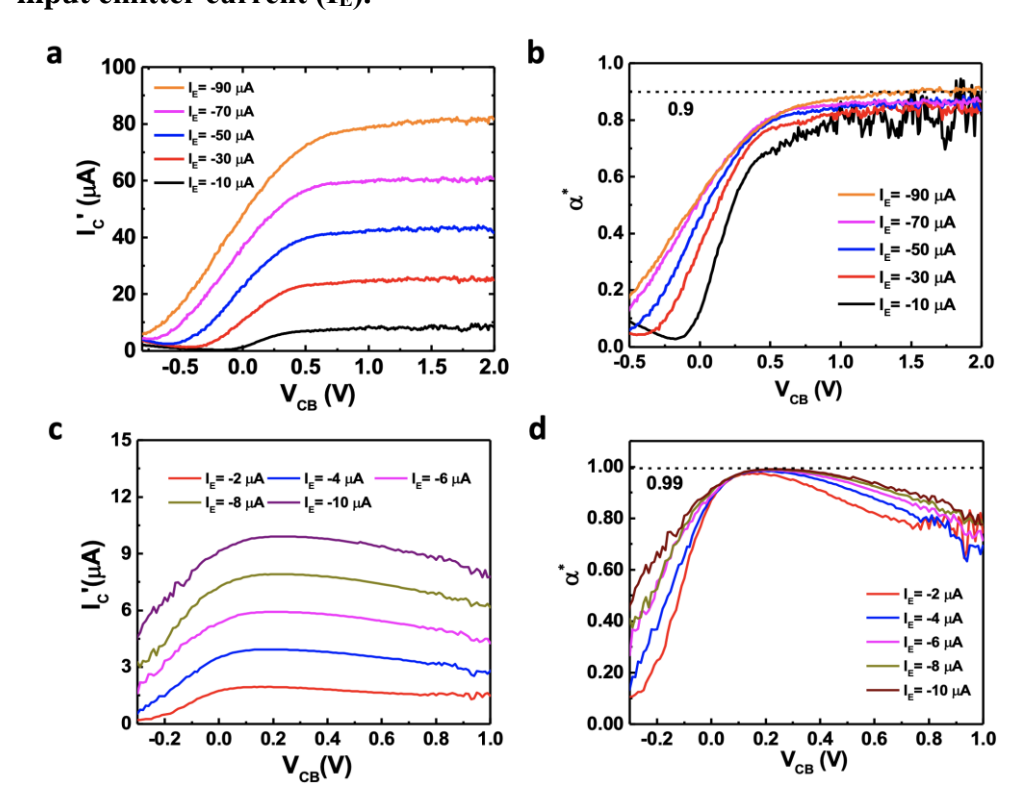


Figure S8. The common base characteristic of both type I and type II GHETs at different input emitter current (I_E). I-V_{CB} curves showing the output collector current (I_C) controlled by various I_E under the common base operation for (a) type I and (b) type II devices. Common base current gain (α^*) as a function of V_{CB} at different values of I_E for (c) type I and (d) type II devices.

The common base characteristic at different input emitter current I_E is shown in Figure S8. I-V_{CB} curves controlled by various I_E for type I and type II devices are shown in Figure S8 (a) and Figure S8 (b) and the common base current gain (α *) as a function of V_{CB} is also demonstrated in Figure S8 (c) and Figure S8 (d) respectively. α * is equal to ($I_C - I_C$ ($I_E = 0A$))/ I_E . Similar saturation behavior of I_C ' and α * at higher V_{CB} is demonstrated for both type I and type II devices.

9. The device-to-device variability of type I and type II devices GHET in the electrical parameters.

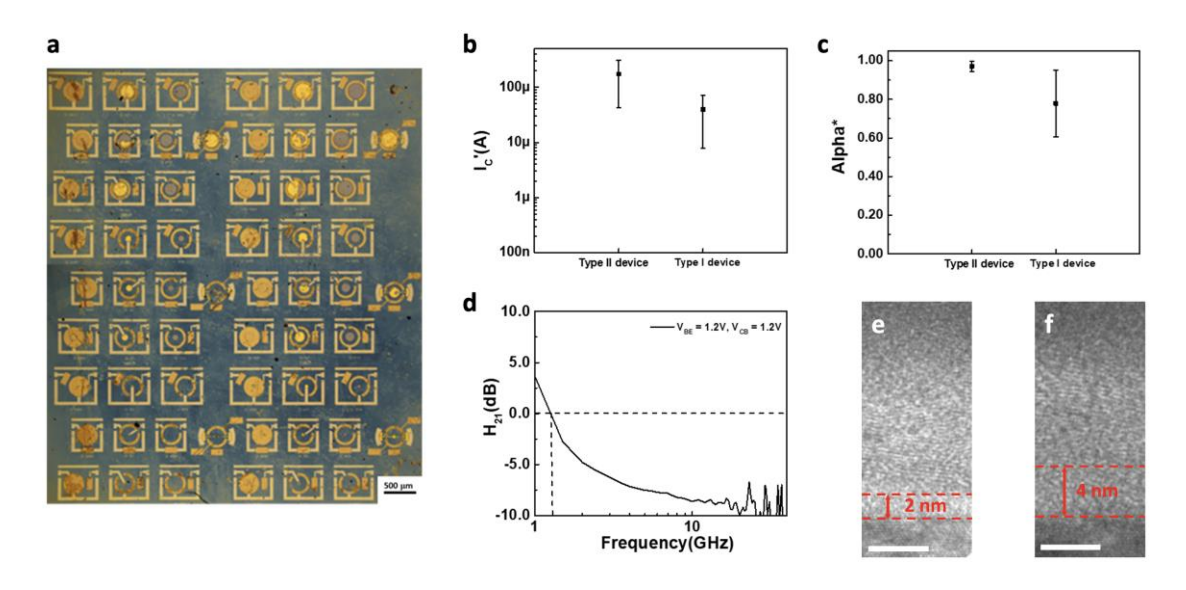


Figure S9. (a) Optical micrograph of the GHET devices. (b) The current (Ic') and (c) the corrected common base current gain (α^*) of type I and type II GHET device. (d) RF measurement of another type II device. (e-f) The TEM images showing two kinds of SiO₂ thicknesses corresponding to the amplified (see Figure S9 (d)) and the unamplified RF characteristics, respectively. The scale bar of (e) and (f) is 5 nm.

We have fabricated 24 GHET devices, in which 18 devices are for both DC and RF measurement while 6 devices are only for DC measurement. There are also extra 18 layouts for the open circuit de-embedding pads, as shown in Figure S9 (a). The design of type I and type II are the same. The device-to-device variability for DC parameters of current (Ic') and corrected common base current gain (α^*) in both type I and type II GHET are shown in Figure S9 (b) and S9 (c), respectively. The reason for the device-to-device deviation is due probably to the variation of growing native silicon dioxide. For example, if we consider FN tunneling model (shown below)⁸ with SiO₂ thickness (d) of 1.2 nm and applied bias (V) of 2V,

$$I(V) = \frac{A_{eff} mq^{3}V^{2}}{8\pi h\phi_{B}d^{2}m^{*}} \exp(\frac{-8\pi\sqrt{2m^{*}}\phi_{B}^{\frac{3}{2}}d}{3hqV})$$

where q, m, m*, h, d, A_{eff} and ϕ_B are elementary charge, electron mass, effective mass $(0.42 \times m \text{ for SiO}_2)$, Plank's constant, SiO₂ thickness, effective area of devices $(5 \times 10^{-6} \text{ cm}^2)$ and barrier height (~2.9 eV), respectively, the current density J_C (= I/ A_{eff}) is close to 280 A/cm². However, if the SiO₂ has a 0.6 nm roughness, which means that the SiO₂ thickness (*d*) could be raised to 1.8 nm, J_C could dramatically decrease to 0.48 A/cm². Therefore, current density is too low to observe a high frequency response.

In RF measurements, there are 6 devices each for type I and type II. However, cutoff frequencies above 1 GHz were observed in only 2 out of 6 of the fabricated type II
devices. Because of either circuit damage or lack of amplification ($H_{21} < 0$) during the
measurement, the cut-off frequencies cannot be obtained for the remaining devices.
After further analyzing the TEM images of the SiO₂ thickness (E-B barrier) of both
measurable and unmeasurable devices, it turns out that the thicknesses of the native
oxide layers for two devices with RF characteristics of 65 GHz (see Figure 4b in main
text) and 1.1 GHz (see Figure S9 (d)) are 1.2 nm (see Figure 1c in main text) and 2 nm
(see Figure S9 (e)), respectively; while for those with unamplified RF phenomena (H_{21}

In order to reduce device variation, a high-quality thin barrier between emitter and base is significant. High quality thin-layered 2D materials (such as h-BN), to replace native SiO₂, would be one of the candidates for improvements in future research.

10. Open de-embedding methods for type II GHET RF measurement

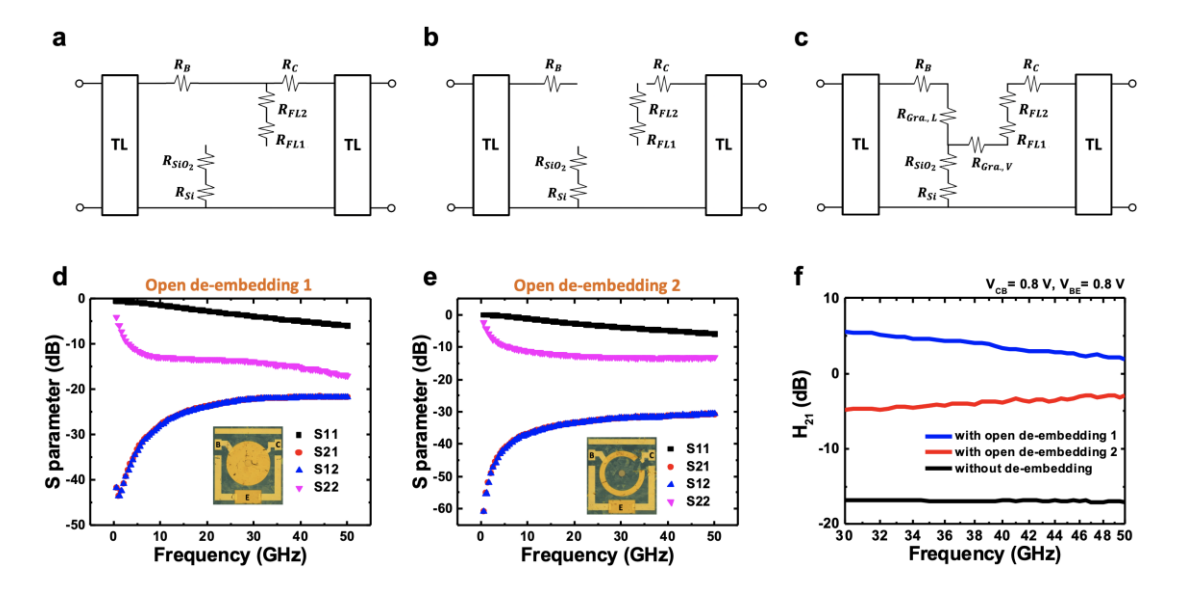


Figure S10. (a-c) Schematics of the equivalent circuit showing the device under test (DUT) connected with the transmission lines (TL) at input and output ports, in which names labeled at certain resistors' subscript correspond to different materials composing the device: (a-b) Two types of open de-embedding approaches where the graphene-base layer is removed; and (c) the representation without open de-embedding. (d-e) The open de-embedded S parameters as a function of frequency for the layout patterns in (a) and (b), respectively. The optical images of the layout patterns are correspondingly shown in the insets of (d) and (e). (f) The H parameter as a function of frequency presenting an amplification behavior by open de-embedding 1 approach.

Figure S10 (a-c) present the equivalent circuits of our graphene-base HET device connected with transmission lines (TL) at input and output ports, in which the device under test (DUT) is denoted as resistors with the names labeled at the subscript corresponding to different materials that composes the DUT. In order to get rid of the additional parasitic capacitances contributed from the interfaces between electrodes and

channel, which may suppress the intrinsic RF performance, we designed and made calibration patterns on the same batch of device fabrication process. At this point, the monolayer graphene was not yet transferred as base terminal. Therefore, the resistor of graphene, $R_{Gra.}$, is removed as shown in the equivalent circuits of the two types of open de-embedding approaches (Figure S10 (a) and Figure S10 (b)). Figure S10 (c) indicates the original equivalent circuit of our measured device without considering open de-embedding method. Here, we take into account both lateral and vertical transport labeled as $R_{Gra.,L}$ and $R_{Gra.,V}$, respectively.

Figure S9 (d) and Figure S9 (e) show the open de-embedded S parameters (scattering parameters) as a function of frequency for two different layout patterns. The corresponding optical images of our measured device are shown in the insets of Figure S9 (d) and Figure S9 (e), respectively. We converted S parameters into Y parameters (admittance parameters) to calculate the de-embedding results by following equations (E3) to (E9).¹⁰

$$\begin{pmatrix} I_1 \\ I_2 \end{pmatrix} = \begin{pmatrix} Y_{11} & Y_{12} \\ Y_{21} & Y_{22} \end{pmatrix} \begin{pmatrix} V_1 \\ V_2 \end{pmatrix} \quad (E3)$$

$$Y_{de-embedding} = Y_{device} - Y_{open1}$$
 (E4)

where Y parameters can be calculated by applying S parameters as shown below:

$$Y_{11} = \frac{((1 - S_{11})(1 + S_{22}) + S_{12}S_{21})}{\Delta_S}Y_0 \quad (E5)$$

$$Y_{12} = \frac{-2S_{12}}{\Delta s} Y_0 \qquad (E6)$$

$$Y_{21} = \frac{-2S_{21}}{\Delta_s} Y_0 \qquad \text{(E7)}$$

$$Y_{22} = \frac{((1+S_{11})(1-S_{22})+S_{12}S_{21})}{\Delta_S}Y_0 \quad (E8)$$

$$Y_0 = \frac{1}{Z_0} \quad (E9)$$

where
$$\Delta_S = (1 + S_{11})(1 + S_{22}) - S_{12}S_{21}$$
, $Z_0 = 50 \ \Omega$.

In Figure S10 (f), the H parameter as a function of frequency indicates that amplification of type II device can be observed with open de-embedding 1 (Figure S10 (d)) instead of the typical layout (Figure S10 (e)).

11. The simulation results for type II GHET RF measurement

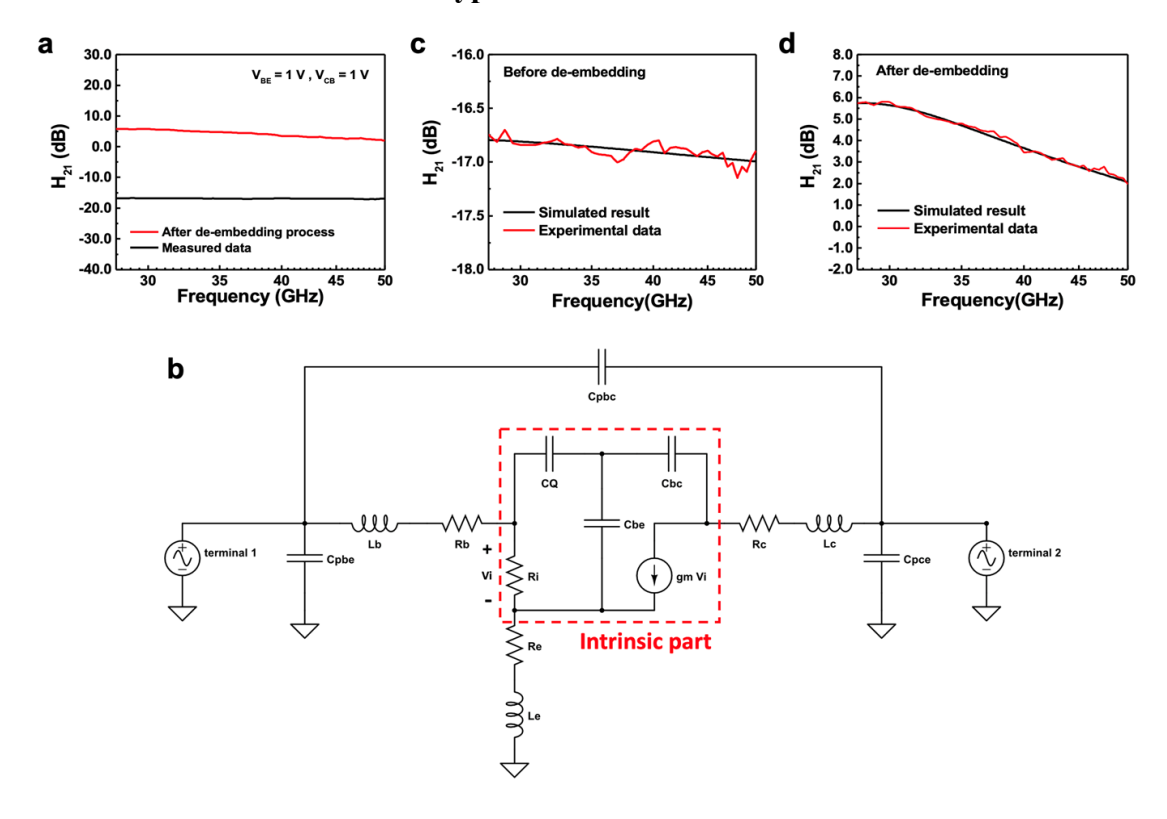


Figure S11 (a) The H₂₁-f characteristic before and after the de-embedding process. (b) The equivalent circuit model of the GHET. The simulated and experimental results (c) before and (d) after de-embedding.

The H₂₁-f characteristic for the measured RF data and the data after de-embedding is shown in Figure S11 (a). We construct the equivalent circuit model (shown in Figure S11 (b)) to figure out the influence of the extrinsic part¹¹ and the intrinsic part¹² in the Advanced Design System software. In this model, Lb, Le, and Lc represent the parasitic electrode inductances; Cpbe, Cpbc, and Cpce are the parasitic pad capacitances due to the pad separately connecting to the base, emitter and collector electrodes. Rb, Re, and Rc signify the parasitic resistances of the base, emitter and collector while Cbe and Cbc are the intrinsic insulator capacitances between the base–emitter, and the base–collector, respectively. CQ is the quantum capacitance of graphene, gm is the intrinsic transconductance and Ri is the intrinsic resistance.

We used this model to simulate our data both before and after the de-embedding process. The results are in good agreement with the experimental data and demonstrated in Figure S11 (c) and Figure S11 (d), respectively. The parameters used are listed in Table S2 and Table S3. This implies that an appropriate de-embedding process is used in our study.

Table S2. The extrinsic elements extracted by equivalent circuit model before and after de-embedding process

	Lb	Lc	Le	Rb	Rc	Re	Cpbc	Cpbe	Срсе
Before	12.94 pH	29.73 nH	27.17 pH	4.23 Ω	71.08 kΩ	3.66 Ω	876 fF	5.50 pF	34.26 pF
After	13.03 pH	6.065 pH	27.15 pH	0.14 mΩ	11.9 Ω	1.3 Ω	356 fF	102 fF	2.96 fF

Table S3. The intrinsic elements extracted by equivalent circuit model before and after de-embedding process

	cq	Cbc	Cbe	Ri	gm
Before	82.78 pF	87.62 pF	4.75 pF	31.49 kΩ	1 mS
After	82.62 pF	87.85 pF	5.05 pF	31.51 kΩ	1 mS

REFERENCES

- 1. Ferrari, A. C.; Basko, D. M. Raman Spectroscopy as a Versatile Tool for Studying the Properties of Graphene. *Nat. Nanotechnol.* **2013**, *8* (4), 235-246.
- 2. Kwon, H.; Garg, S.; Park, J. H.; Jeong, Y.; Yu, S.; Kim, S. M.; Kung, P.; Im, S. Monolayer MoS₂ Field-Effect Transistors Patterned by Photolithography for Active Matrix Pixels in Organic Light-Emitting Diodes. *NPJ 2D Mater. Appl.* **2019**, *3* (1), 9.
- 3. Hsiou, Y.-F.; Yang, Y.-J.; Stobinski, L.; Kuo, W.; Chen, C.-D. Controlled Placement and Electrical Contact Properties of Individual Multiwalled Carbon Nanotubes on Patterned Silicon Chips. *Appl. Phys. Lett.* **2004**, *84* (6), 984-986.
- 4. Xia, F.; Perebeinos, V.; Lin, Y.-m.; Wu, Y.; Avouris, P. The Origins and Limits of Metal–Graphene Junction Resistance. *Nat. Nanotechnol.* **2011**, *6* (3), 179-184.
- 5. Russo, S.; Craciun, M.; Yamamoto, M.; Morpurgo, A.; Tarucha, S. Contact Resistance in Graphene-Based Devices. *Physica E Low Dimens. Syst. Nanostruct.* **2010**, 42 (4), 677-679.
- 6. Sarker, B. K.; Khondaker, S. I. Thermionic Emission and Tunneling at Carbon Nanotube–Organic Semiconductor Interface. *ACS nano* **2012**, *6* (6), 4993-4999.
- 7. Beebe, J. M.; Kim, B.; Gadzuk, J. W.; Frisbie, C. D.; Kushmerick, J. G. Transition from Direct Tunneling to Field Emission in Metal-Molecule-Metal Junctions. *Phys. Rev. Lett.* **2006**, *97* (2), 026801.
- 8. Lee, G.-H.; Yu, Y.-J.; Lee, C.; Dean, C.; Shepard, K. L.; Kim, P.; Hone, J. Electron Tunneling Through Atomically Flat and Ultrathin Hexagonal Boron Nitride. *Appl. Phys. Lett.* **2011**, *99* (24), 243114.
- 9. Brar, B.; Wilk, G.; Seabaugh, A. Direct Extraction of the Electron Tunneling Effective Mass in Ultrathin SiO₂. *Appl. Phys. Lett.* **1996**, *69* (18), 2728-2730.

- 10. Da Silva, E., *High Frequency and Microwave Engineering*. 1st ed.; Oxford Butterworth-Heinemann, Newnes: 2001.
- 11. Le, Y.; Yingkui, Z.; Sheng, Z.; Lei, P.; Ke, W.; Xiaohua, M. Small-Signal Model Parameter Extraction for AlGaN/GaN HEMT. *J. Semicond.* **2016**, *37* (3), 034003.
- 12. Mehr, W.; Dabrowski, J.; Scheytt, J. C.; Lippert, G.; Xie, Y.-H.; Lemme, M. C. Ostling, M.; Lupina, G., Vertical Graphene Base Transistor. *IEEE Electron Device Lett.* **2012**, *33* (5), 691-693.